RSC Advances

PAPER

View Article Online
View Journal | View Issue

Cite this: *RSC Adv.*, 2024, **14**, 35090

Effective BPA degradation in water: the integration of bimetallic UiO-66 Ce–Zr†

Leidy Marcela Gallo,[a] Juan L. Obeso,[ab] Nora S. Portillo-Vélez,[c] Carlos E. Garduño-Albino,[c] Catalina V. Flores,[a] Leonardo Herrera-Zuñiga,[c] Alejandro Islas-Jácome,[c] Ricardo A. Peralta *[c] and Carolina Leyva *[a]

Received 7th September 2024
Accepted 21st October 2024

DOI: 10.1039/d4ra06460g

rsc.li/rsc-advances

In this work, a bimetallic MOF UiO-66 Ce–Zr to degrade bisphenol A (BPA) in water was synthesised. The material exhibited a remarkable degradation efficiency of 84.3% under UV irradiation for 240 minutes. Combining cerium (Ce) and zirconium (Zr) in the MOF structure enhanced the catalytic activity and reinforced its structural stability. Comprehensive characterisation was performed using PXRD, FT-IR, SEM-EDS, XPS, and N_2 adsorption–desorption isotherms. Scavenger tests confirmed that hydroxyl ($^{\bullet}OH$) and superoxide ($^{\bullet}O_2^-$) radicals played a crucial role in the photocatalysis. The material demonstrated excellent reusability, maintaining high performance over three cycles with minimal structural changes. Furthermore, a toxicological evaluation of the degradation by-products was conducted using UPLC-MS, reaffirming the potential of the material as an efficient water treatment system. This study underscores the potential of UiO-66 Ce–Zr as a stable and effective photocatalyst for water treatment applications, particularly in removing emerging pollutants such as BPA.

Introduction

Water, the lifeblood of our planet, is gravely under siege. Despite its indispensable role, our water bodies are increasingly and alarmingly contaminated, which is a crisis fueled mainly by human activities, such as agriculture, industry, and urban development.[1] Among the culprits are emerging contaminants (ECs) and unregulated organic compounds like pesticides, pharmaceuticals, and endocrine disruptors (EDCs).[2] Classic EDCs include pesticides, herbicides, phthalates, and bisphenols. Bisphenol A (BPA) is a synthetic chemical agent recognised for its alarming ability to disrupt the endocrine system. Its uses include manufacturing essential consumer products, such as water bottles, baby bottles, canned goods, and various plastics.[3] BPA has been associated with a myriad of diseases, such as cancer, polycystic ovary syndrome, depression, obesity, insulin resistance, reproductive disorders, and cardiovascular problems.

Different techniques have been explored to remove contaminants from water sources, including adsorption, coagulation, filtration, and sedimentation.[4] Although these techniques remove contaminants from water, they do not chemically degrade or destroy them, which can result in waste that requires further treatment. On the other hand, heterogeneous photocatalysis has proven to be an environmentally friendly, cost-effective, and efficient tool for degrading contaminants in water.[5] This technique relies on semiconductor photocatalysis, which generates reactive oxygen species, such as superoxide radicals ($^{\bullet}O_2^-$) and hydroxyl radicals ($^{\bullet}OH$), which are essential for degradation.[6] Additionally, materials such as zeolites, graphene oxide, and carbon nanomaterials have been evaluated and widely used for degradation.[7,8] However, in some cases, these materials exhibit instability, low efficiency, lack of reusability, and recombination; these materials need further research to overcome these limitations.

A novel alternative to tackle this problem is using metal–organic frameworks (MOFs), which contain metal nodes coordinated to organic ligands, forming a bi- or tri-dimensional structure.[9] MOFs are notable for their large surface area, design flexibility, high porosity, and elevated volume.[10] These characteristics make them highly versatile in energy storage, catalysis, and contaminant degradation applications.[11,12] In water remediation, MOFs have been employed to degrade BPA. For example, Liu *et al.*[13] employed enzyme encapsulation within the MOF (HRP-ZIF-8), achieving a high efficacy of 94.7% in BPA degradation. Despite these promising results, the high cost of

[a]*Instituto Politécnico Nacional, Centro de Investigación en Ciencia Aplicada y Tecnología Avanzada, Laboratorio Nacional de Ciencia, Tecnología y Gestión Integrada del Agua, Legaria 694, Col. Irrigación, Miguel Hidalgo, 11500, CDMX, Mexico. E-mail: zleyva@ipn.mx*

[b]*División de Ingeniería en Sistemas Automotrices, Tecnológico de Estudios Superiores del Oriente del Estado de México (TESOEM), Tecnológico Nacional de México, Estado de México 56400, Mexico*

[c]*Departamento de Química, División de Ciencias Básicas e Ingeniería, Universidad Autónoma Metropolitana (UAM-I), 09340, Mexico. E-mail: rperalta@izt.uam.mx*

† Electronic supplementary information (ESI) available: Instrumental techniques and characterization. See DOI: https://doi.org/10.1039/d4ra06460g

synthesis is a significant challenge for its commercial application. Conversely, Guan *et al.*[14] conducted a modification that involved doping with iron in the MOF UiO-66 Zr. Cerium (Ce) and zirconium (Zr) are two metals that stand out in materials science and environmental chemistry. Ce is notable in various applications as it was the first lanthanide to be discovered and can switch between oxidation states +3 and +4, making it an ideal component in catalytic processes. This property highlights its importance in oxidation and reduction reactions, making it a key element in degrading organic pollutants like phenol and bisphenol A.[15,16] The choice of cerium in this work optimises the catalytic reactivity and provides cost and efficiency benefits, helping to address pollution challenges.[17,18] Conversely, Zr is known for its exceptional corrosion resistance and thermal stability. For instance, zirconium dioxide (ZrO_2) has established itself as a catalytic support in the oxidation of organic compounds such as phenol, contributing to the remediation of industrial wastewater. Additionally, zirconium is part of nanostructures that enhance catalytic processes due to its ability to withstand extreme conditions without losing efficiency.[16,19,20]

Based on this, incorporating this metal mixture could enhance the degradation performance. Hence, this study introduces a bimetallic MOF UiO-66 Ce–Zr as a potential game-changer in the effective degradation of BPA in water solutions. The MOF material was subjected to rigorous characterisation using powder X-ray diffraction (PXRD), Fourier-transform infrared spectroscopy (FT-IR), scanning electron microscopy with energy-dispersive X-ray spectroscopy (SEM-EDX), X-ray photoelectron spectroscopy (XPS), and N_2 adsorption. Moreover, the results show a degradation efficiency of 84.3%, achieved at a BPA concentration of 50 ppm after just 4 hours. This could indicate the potential of the bimetallic MOF UiO-66 Ce–Zr in the water treatment field.

Experimental section

Materials

Detailed information on the materials is available in Section S1.†

Synthesis of the MOFs

Synthesis of the MOF UiO-66 Zr. The MOF UiO-66 Zr was synthesized using the solvothermal method. During the synthesis, 2.5 mmol of terephthalic acid was dissolved in 20 mL of DMF, and the mixture was stirred for approximately 10 minutes. Next, 2.38 mmol of $ZrOCl_2 \cdot 8H_2O$ was added and stirred in the mixture for 10 minutes. The solution was transferred to a 100 mL Teflon vessel and heated to 150 °C for 24 hours. After cooling, the solid was washed three times with DMF and three times with acetone. Finally, we dried the solid at 70 °C.

Synthesis of the MOF UiO-66 Ce. The method described by N. Stock *et al.*[21] was followed to synthesize the MOF UiO-66 Ce. A 1.25 mmol quantity of terephthalic acid was dissolved in 7.5 mL of DMF and stirred for 10 minutes. Similarly, 1.5 mmol of Ce $(NH_4)_2(NO_3)_6$ was stirred in 2.5 mL of water for about 10 minutes. The two solutions were mixed and transferred to a 50 mL Teflon vessel and subsequently heated to 100 °C for 15 minutes. After the product had cooled, it was washed with DMF and methanol three times.

Synthesis of the MOF UiO-66 Ce–Zr. The synthesis was carried out using the solvothermal method described by Sharma *et al.*[22] Initially, two mmol of terephthalic acid was dissolved in 10 mL of a DMF–water mixture in a 1 : 2 ratio, and the mixture was stirred for approximately 10 minutes. Then, two mmol of $ZrOCl_2 \cdot 8H_2O$ and one mmol of $Ce(NH_4)_2(NO_3)_6$ were added to the mixture and stirred for 5 minutes. The solution was transferred to a 150 mL Teflon vessel and heated to 150 °C for 72 hours. After cooling, the product was washed three times with DMF and acetone. Finally, the obtained solid was dried at 150 °C for 24 hours.

Analytical instruments

Detailed information on the instrumental techniques is available in Section S1.†

Electrochemical characterisation

Electrochemical impedance spectroscopy (EIS) studies were conducted in a three-electrode cell to evaluate the semiconductors electrochemically. Electrodes of fluorine-doped tin oxide (FTO) glass with a specific area of 0.7×0.7 cm^2 were used. These electrodes underwent cleaning cycles by sonication in Milli-Q water and ethanol, each for 30 minutes, followed by drying at 75 °C for an hour Rangel-Váquez *et al.*[23] previously explained how to make a suspension of UiO-66 Ce, UiO-66 Zr, and UiO-66 Ce–Zr, which are artificial MOFs. It was simple to use the drop-casting method to evenly spread 8 mg of the MOF, 1.5 mL of ethanol, and 150 μL of Nafion on the FTO glass's active surface. A 0.5 M aqueous sodium sulfate solution was used as the supporting electrolyte, with a platinum counter electrode and an Ag/AgCl reference electrode. The semiconducting properties of the photocatalyst films were determined by analysing Mott–Schottky plots at various potentials.

Photocatalytic tests for bisphenol A degradation

The photocatalytic activity of the derived MOFs UiO-66 was evaluated for the degradation of BPA (Fig. S1†). This evaluation was carried out in a cylindrical double-walled photoreactor with a capacity of 250 mL, maintaining room temperature with constant stirring and air bubbling in each experiment. A mercury lamp (a PenRay lamp with primary energy at 254 nm) was used as the UV irradiation source. The photocatalytic tests were conducted by adding 50 mg of MOFs (UiO-66) to 50 mL of a BPA solution (50 ppm). Before initiating the photocatalytic reaction, the solution containing the photocatalyst was left to stand for 30 minutes without turning on the lamp to achieve adsorption–desorption equilibrium on the catalyst surface. After the equilibrium period, the lamp was turned on to begin the contaminant degradation. The BPA degradation was then monitored every hour for 4 hours. A Waters ACQUITY UPLC H-Class Series ultra-high-performance liquid chromatography system was used to quantify the BPA concentration. A quadrupole mass detector (ACQUITY QDa) with electrospray ionization

(ESI) was used to determine the by-products in the UPLC system.

The following equation was used to determine the efficiency of photodegradation:

$$\text{Photodegradation efficiency } (\%) = \left(1 - \frac{C}{C_0}\right) \times 100 \quad (1)$$

Scavenger tests

Whole and radical trapping tests were conducted to thoroughly investigate the reactive oxygen species (ROS) responsible for BPA degradation. Different scavenging agents were used (Fig. S2†), such as salicylic acid (SA) to study the hydroxyl radicals ($^{\bullet}OH$). For example, it was demonstrated that the reaction of salicylic acid with $^{\bullet}OH$ produces hydroxylated derivatives such as 2,3-dihydroxybenzoic acid, which can be quantified by UV-Vis spectrophotometry, allowing the estimation of $^{\bullet}OH$ concentration,[24] citric acid (CA) to identify photogenerated holes (h^+), *p*-benzoquinone (PBQ) to determine the effect of superoxide radicals ($^{\bullet}O_2^-$), and DMSO to examine the role of electrons (e^-) in the process. The concentration of these agents in the photocatalytic reaction system was set at 1 mM, surpassing the concentration of BPA. Each agent was added independently, adhering to the previously described degradation process in Section S1.† The variation in the photocatalytic efficiency of bisphenol A (BPA) with the addition of each agent was subsequently evaluated, thereby determining their specific contributions to the degradation process.[25]

Computational analysis methodology

To achieve optimal performance at the PBE/cc-pVTZ level, a water solvent model must be added based on the density of charge (SMD). The BPA ligand was tuned using the Gaussian 09 quantum chemistry software. The GGA Perdew–Burke–Ernzerhof (PBE) approach has been used in a significant number of first-principles (DFT) material research studies, which led to the selection of this particular computational level. The foundation set was selected due to attempts to balance cost and accuracy.[26] Several different sources, such as the Cambridge Structural Database (CSD) (**https://www.ccdc.cam.ac.uk/**), were used to acquire the structures of the MOFs that are the focus of this investigation. Immediately after the docking procedure, the same degree of theory was used to compute the energetic interactions that took place between the MOF and the BPA. In the MOF-BPA docking process, AutoDock Vina 1.1.2 was employed to estimate the binding score between BPA and the MOF. One hundred iterations of the Lamarckian evolutionary algorithm were carried out, resulting in one hundred optimum conformations that were suitable for BPA screening grid maps. We used Chimera to depict all BPA-MOF complexes.[27] The volumes of MOF and ligand were calculated with the MoloVol software.[28] The conformation that possessed the lowest score was selected. We used the SwissADME and ProTox-3.0 software to carry out the analysis of the pharmacokinetic and toxic characteristics (ADMETox) of the degradation products to estimate their toxicity and ecotoxicity.

Results and discussion

Characterisation of MOFs UiO-66

The materials were synthesised using the solvothermal method. The XRD patterns (Fig. S3†) corroborate the pure phase of UiO-66 Ce and UiO-66 Zr. Moreover, MOF UiO-66 Ce–Zr showed index patterns in the pristine UiO-Ce and UiO-Zr.[22] The FT-IR spectra of the three synthesised MOFs (Fig. S4†) show the characteristic bands for the UiO-66 materials. The Ce–O bond stretching vibrations are seen at 545 cm^{-1}. Between 750 and 680 cm^{-1}, the symmetric bands correspond to the Zr–O bond vibrations. The peaks at 1590 and 1400 cm^{-1} were associated with the antisymmetric and symmetric vibrations of the carboxylate groups.[29] Furthermore, using the SEM technique, a well-defined rod-like morphology of the MOF UiO-66 Ce–Zr was observed (Fig. S7†), which yields similar results to those reported by Sharma *et al.*[22] Elemental composition was performed to corroborate the presence of carbon (C), oxygen (O), cerium (Ce), and zirconium (Zr), corroborating the effectiveness of the synthesis. Elemental mapping EDS analysis confirmed the Ce : Zr ratio 1 : 2. Based on the N_2 adsorption–desorption isotherm (Fig. S8†) for the MOF UiO-66 Ce–Zr, the BET surface area and pore volume were calculated, displaying 328 $m^2\ g^{-1}$ and 0.32 $cm^3\ g^{-1}$, respectively.

The electrochemical characterisation was carried out to calculate the flat-band potential (EFB) and corroborate the type of semiconductor (Fig. S9†) presented by Mott–Schottky (M–S). In each case, a positive slope in the M–S curve is observed. This is characteristic of an n-type semiconductor, indicating the presence of an excess of electrons in the material. The results suggest that the materials are suitable photocatalytic materials because they make more charge carriers (electron–hole pairs) available, which are necessary to break down contaminants.[30] For the UiO-66 Ce MOF, the energy level of the conduction band (CB) is more negative than the standard redox potential of superoxide ($E(O_2/^{\bullet}O_2^-) = -0.33$ V *vs.* NHE). This allows superoxide radicals ($^{\bullet}O_2^-$) to degrade BPA more efficiently. In contrast, the valence band (VB) has a less positive potential than the redox potential of hydroxyl radicals ($E(H_2O/^{\bullet}OH) = 2.40$ V *vs.* NHE), which prevents the generation of hydroxyl radicals ($^{\bullet}OH$). Although the MOF UiO-66 Zr can generate superoxide radicals, its high VB energy reduces hydroxyl radical generation. Conversely, combining the properties of Ce and Zr metals in the bimetallic MOF UiO-66 Ce–Zr improves the photocatalytic properties. It shows a band gap of 3.2 eV, suggesting that UiO-66 Ce–Zr exhibits excellent stability under ultraviolet irradiation, similar to its components. Also, UiO-66 Ce–Zr CB at −0.211 V *vs.* NHE is enough to break down molecular oxygen and create superoxide radicals. At the same time, the VB, which is at +2.99 V *vs.* NHE, allows water oxidation to produce hydroxyl radicals following the scavenger test.[31]

Photocatalytic activity

Considering this analysis, our first approach to perform photocatalytic experiments was to use Uio-66 Ce. This material has been previously reported as possessing excellent photocatalytic

properties because of the abundant Ce^{4+} ions, which can change oxidation states from Ce^{4+} to Ce^{3+}.[21] The material was effectively synthesised and employed for BPA degradation in the presence of UV light over 4 hours. The degradation kinetics were monitored hourly, commencing with a half-hour stage of adsorption in the absence of light, followed by hourly measurements until the completion of the four hours. The results were remarkable, with a degradation efficiency of 94%, which is notable considering the quick and straightforward synthesis of the material. Nevertheless, PXRD confirmed that the material structure lacks crystallinity (Fig. S12†), making its reuse unfeasible. These findings indicate that, although the Ce^{4+} MOF has potential in photocatalysis, the lack of stability is an important consideration to be addressed for its potential use for the degradation of contaminants.[32]

MOF UiO-66 Zr stands out due to the presence of Zr^{4+} species, which gives it greater resilience. This robustness helps to overcome the structural stability issues found in UiO-66 Ce. The UiO-66 framework possesses a characteristic connection of zirconium clusters. Each Zr_6 cluster is linked to 12 BDC linkers, forming a three-dimensional cubic network that provides the material with remarkable thermal and chemical stability and well-defined porosity.[33] This MOF was successfully synthesised and then subjected to the same conditions for BPA degradation (Fig. 1a and b), achieving a remarkable degradation efficiency of 74%. While the percentage is smaller than the cerium MOF, PXRD structural testing (Fig. S13†) demonstrated that the material maintains its crystalline structure without any alterations, making it easier to reuse.[34]

Inspired by this robustness of the UiO-66 Zr material, a bimetallic MOF UiO-66 Ce–Zr was synthesised to merge the catalytic benefits of cerium MOF with the structural durability of zirconium MOF. This strategy aims to exploit the outstanding photocatalytic properties of Ce^{4+} in combination with the durability of Zr^{4+}, resulting in a material that is not only highly effective in breaking down pollutants like BPA but also maintains its crystalline structure (Fig. 1c), enabling its reuse in long-term applications. The material also maintained the rod-like morphology after the degradation process (Fig. S11†). The N_2 adsorption–desorption isotherm (Fig. S15†) indicates preserving the BET surface area (286.19 $m^2\ g^{-1}$). Moreover, studies conducted by Y. Wang *et al.*[35] highlight the potential of bimetallic MOFs, particularly when incorporating Zr, as this imparts superior stability and efficiency to the material in degradation processes. By synthesising and evaluating the bimetallic MOF UiO-66 Ce–Zr, we discovered that it achieved an efficiency of 84.3% in the photodegradation of BPA, which outperformed different materials (Table S3†). This efficiency surpassed that of Zr MOF (74%) but fell short of the efficiency of MOF Ce (94%).

This performance demonstrates the ideal equilibrium between the stability of Zr and the catalytic reactivity of Ce. Additionally, a study was conducted to examine the reusability of MOF UiO-66 Ce–Zr, which demonstrated its chemical stability and exceptional effectiveness in removing BPA. The recovered catalyst was subjected to three more reaction cycles to evaluate its potential for reuse (Fig. 1d). The results

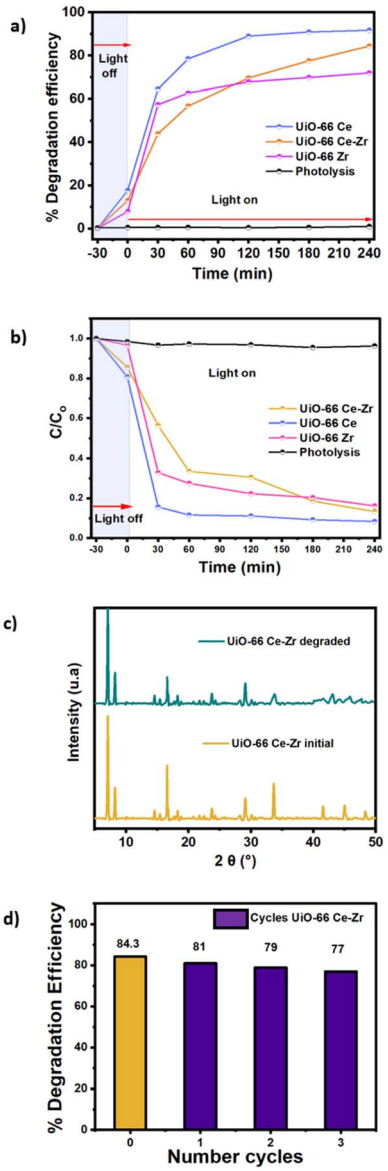

Fig. 1 (a and b) Photodegradation efficiency of the MOFs UiO-66 in kinetic studies without and with a lamp. (c) PXRD patterns of the initial MOF UiO-66 Ce–Zr and degraded MOF UiO-66 Ce–Zr. (d) Recyclability of the MOF UiO-66 Ce–Zr for three cycles.

demonstrated that MOF UiO-66 Ce–Zr exhibited BPA conversion rates of 82%, 79%, and 77% for the first, second, and third cycles, respectively. This suggests a gradual decline in the catalytic efficiency of the MOF with each successive cycle. The minor drop in efficiency may be attributed to alterations in the crystallinity of the material (Fig. S14†).

Pseudo-first-order and pseudo-second-order kinetics models were used to describe the degradation of BPA using UiO-66 Ce–Zr. The material shows a superior overall fit, particularly in the pseudo-second-order model (Fig. S10†), with an R^2 value of 0.96 (Table S2†). This implies that the degradation process of BPA pollutants followed the pseudo-second-order kinetics model, suggesting that the degradation of BPA is driven by rapid adsorption.[36] This is in line with the high degradation efficiency achieved at 240 min. The presence of both Ce and Zr in the MOF

enhances its stability and degradation efficiency. The degradation process involves the initial adsorption of BPA, followed by interaction with radicals formed on the catalyst's surface. Thus, UiO-66 Ce–Zr exhibits great potential for use in pollutant treatment.

Scavenger test

Scavenging tests were performed to identify the reactive oxygen species (ROS) responsible for the photocatalytic degradation activities, such as superoxide ($^{\bullet}O_2^-$) radicals, positively charged holes (h^+), hydroxyl radicals ($^{\bullet}OH$) and (e^-). The $^{\bullet}O_2^-$, h^+, $^{\bullet}OH$, and e^- scavengers used for the study were *p*-benzoquinone (PBQ), citric acid (CA), salicylic acid (SA), and dimethyl sulfoxide (DMSO), respectively. Fig. 2 illustrates the effect of chemical scavengers on the photocatalytic activity of MOF UiO-66 Ce–Zr.

The photodegradation efficiency of BPA was inhibited when SA was added, suggesting that $^{\bullet}OH$ played an essential role in the photodegradation of BPA. With the addition of PBQ, the photodegradation rate of BPA also decreased, suggesting that $^{\bullet}O_2^-$ also plays a crucial role in photocatalytic degradation. CA causes a minor effect in decreasing photoactivity, and h^+ has a lower participation. However, no significant decrease is seen in the photocatalytic degradation rate of BPA in the presence of DMSO, suggesting that the contribution of e^- is minimal. Thus, it can be inferred that the $^{\bullet}OH$, $^{\bullet}O_2^-$ and h^+ radicals took part in the photodegradation of BPA with MOF UiO-66 Ce–Zr under UV light irradiation, with significant contributions from $^{\bullet}OH$ and $^{\bullet}O_2^-$ as supported by other studies,[37,38] rather than h^+.

XPS characterisation was performed to confirm the stability of UiO-66 Ce–Zr MOF. The survey analysis (Fig. S16†) shows no significant changes after BPA photodegradation. The high-resolution XPS spectra of C 1 s (Fig. 3a) exhibit peaks at 284.7, 286.1, 288.4, and 289.9 eV related to C=C in the aromatic rings, C–OH, –C=O and π–π*. After the photoreaction, the peaks shift to 284.6, 285.6, 288.6, and 289.6 eV, respectively. The most evident change (0.5 eV) in the binding energy to lower energies was for the peak associated with C–OH. For the O 1 s region (Fig. 3b), the displayed peaks at 530.1, 531.5, and 533.3 eV are related to M-O, C–H/C=O, and C=O, respectively. After BPA photodegradation, only the peaks of C–H/C=O and C=O shifted to lower energies by 0.2 eV and 0.6 eV, respectively, which is associated with increased electron density due to organic subproducts. The high-resolution XPS spectra of Zr 3d (Fig. 3c) show two peaks at around 182.6 and 184.9 eV ($\Delta = 2.3$ eV), which can be assigned to Zr $3d_{5/2}$ and Zr $3d_{3/2}$, respectively.[39] After the photoreaction, a slight shift of 0.1 eV to higher binding energies was observed.

The high-resolution XPS spectra of Ce 3d (Fig. 3d) display a significant spin–orbit separation between the $3d_{5/2}$ and $3d_{3/2}$ emission features ($\Delta = 18.6$ eV). The presence of Ce^{3+} can be identified by two peaks associated with each spin-orbital (v^0/v^1 and u^0/u^1). These two characteristic peaks present binding energies of 883.9 eV and 902.5 eV. The "v" peaks are associated with the $3d_{5/2}$ spin–orbit peaks and the "u" peaks with the $3d_{3/2}$ peaks. The peak shift in the Ce spectra was 0.3 eV to lower binding energies.[40] These shifts in the binding energies for Zr and Ce 3d to lower values can be related to a change in the chemical environment of the metal centres in UiO-66.

Computational analysis methodology

Based on these results, density functional theory (DFT) and docking simulations were used to examine the interaction between BPA and the octahedral and tetrahedral pores of the

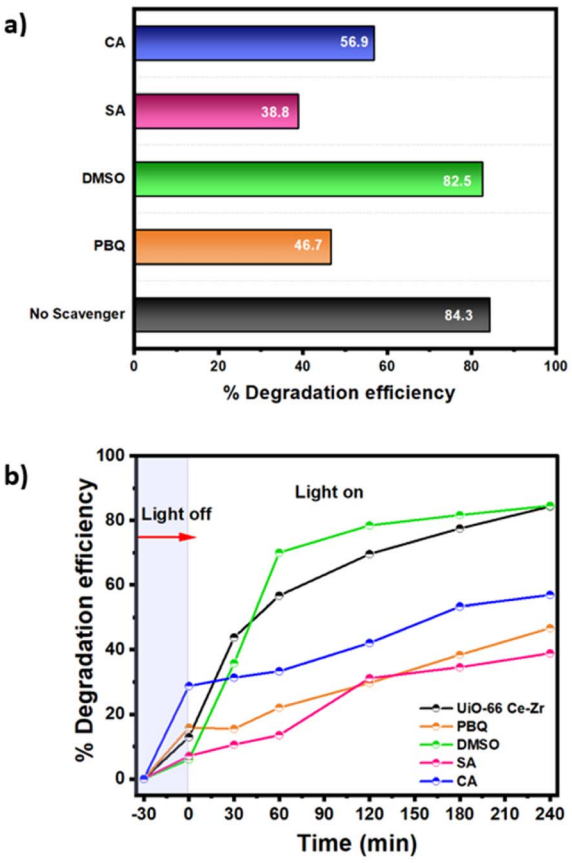

Fig. 2 (a) Scavenger test of the MOF UiO-66 Ce–Zr. (b) Photodegradation efficiency of the MOFs UiO-66 Ce–Zr in kinetic studies without and with a lamp using the scavenger test.

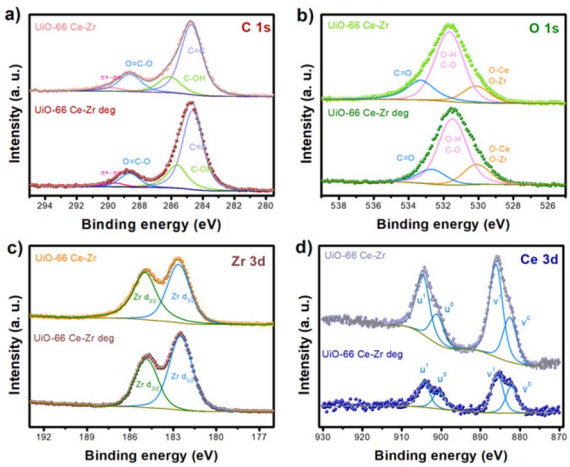

Fig. 3 High-resolution XPS spectra before and after BPA photodegradation of (a) C 1 s, (b) O 1 s, (c) Zr 3d, and (d) Ce 3d.

UiO-66 framework. The calculated aggregate volumes and surface areas of the UiO-66 pores and the amount of BPA provide a valuable understanding of the observed variations in binding behaviour. More precisely, the octahedral volume of 3428.016 Å^3 and the surface area of 69.34754 Å^2 provided a better spatial fit for BPA, which in turn had a volume of 324.6 Å^3 (Table S9†). The significant volume-to-surface-area ratio of this material promotes efficient interactions, which is shown by the negative binding energy and emphasises its compatibility with BPA. Also, docking investigations were carried out (Fig. S17†) to achieve an accurate geometric recognition between BPA and the octahedral pores of the framework, yielding favourable interaction energy. Conversely, the tetrahedral conformation shows a less satisfactory alignment within the pore, consistent with the positive binding energy obtained from the DFT calculations (Table S10†).

In an effort to understand the photocatalytic by-products generated during the degradation of BPA, an analysis of the degraded samples was conducted using UPLC-MS (Ultra-performance liquid chromatography-mass spectrometry). The reaction pathway for the photocatalytic degradation of bisphenol A with UiO-66 Ce–Zr illuminated with UV light is illustrated in Fig. S18.† The most abundant by-products were successfully identified, such as (2*Z*)-but-2-enedioic acid; 5-[2-(4-hydroxyphenyl) propan-2-yl] benzene-1,2,3-triol; and phenol (see Table S13† for the complete by-products after degradation). Furthermore, a toxicology *in silico* study of the degradation products was carried out, with but-2-enedioic acid and 5-[2-(4-hydroxyphenyl) propan-2-yl] benzene-1,2,3-triol being less harmful than BPA. Conversely, phenol has a high degree of intestinal permeability, has increased toxicity (LD_{50}: 270 mg kg^{-1}), and poses the risks of neurotoxicity and ecotoxicity (see ESI† for details). These results highlight the importance of analysing the products formed after the degradation of BPA, as we can produce by-products that could be not only less toxic but also more lethal, such as phenol, than the original compound.

Conclusions

In summary, this study highlights the effective degradation of BPA from water solution. Incorporating a bimetallic MOF material UiO-66 Ce–Zr boosted the chemical stability of the degradation processes, displaying a remarkable degradation efficiency of 84.3% under UV irradiation for 240 minutes. The strength and efficacy of the MOF Ce–Zr UiO-66 catalyst have been successfully demonstrated, as it retains its catalytic activity over three cycles. The degradation by-products analysis was conducted using UPLC-MS, and a toxicological evaluation confirmed the potential of the material for safe and efficient water treatment. This makes it a promising alternative for degradation contaminants like BPA in aqueous environments, highlighting its potential for water treatment applications.

Data availability

The data supporting this article have been included as part of the ESI.†

Conflicts of interest

There are no conflicts to declare.

Acknowledgements

L. M. G. and J. L. O. thank CONACYT for PhD fellowships (1272650 and 1003953). C. E. G. A. thanks CONACYT for the Master fellowship (1331235). R. A. P., C. E. G. A. and L. D. H. Z. thank the Laboratorio de Supercómputo y Visualización en Paralelo (Yoltla) for providing the computational resources to prepare this work. C. L. thanks the IPN projects (20242829, 20241189, 20231282 and 20232785).

References

1 M. J. Currell and D. Han, *Environment: Science and Policy for Sustainable Development*, 2017, **59**, 16–29.
2 V. Geissen, H. Mol, E. Klumpp, G. Umlauf, M. Nadal, M. Van Der Ploeg, S. E. A. T. M. Van De Zee and C. J. Ritsema, *Int. Soil Water Conserv. Res.*, 2015, **3**, 57–65.
3 H. Gao, B.-J. Yang, N. Li, L.-M. Feng, X.-Y. Shi, W.-H. Zhao and S.-J. Liu, *Medicine*, 2015, **94**, e211.
4 S. Zhang, J. Wang, Y. Zhang, J. Ma, L. Huang, S. Yu, L. Chen, G. Song, M. Qiu and X. Wang, *Environ. Pollut.*, 2021, **291**, 118076.
5 S. Garcia-Segura and E. Brillas, *J. Photochem. Photobiol., C*, 2017, **31**, 1–35.
6 C. Belver, J. Bedia, A. Gómez-Avilés, M. Peñas-Garzón and J. J. Rodriguez, in *Nanoscale Materials in Water Purification*, Elsevier, 2019, pp. 581–651.
7 N. Munir, A. Javaid, Z. Abideen, B. Duarte, H. Jarar, A. El-Keblawy and M. S. Sheteiwy, *Environ. Sci. Pollut. Res.*, 2023, **31**, 1695–1718.
8 O. O. Oluwasina and A. A. Adelodun, *Nanotechnol. Environ. Eng.*, 2024, **9**, 389–409.
9 C. Pettinari and A. Tombesi, *Inorganics*, 2023, **11**, 65.
10 M.-A. Gatou, I.-A. Vagena, N. Lagopati, N. Pippa, M. Gazouli and E. A. Pavlatou, *Nanomaterials*, 2023, **13**, 2224.
11 J. L. Obeso, V. B. López Cervantes, C. V. Flores, C. García-Carvajal, C. E. Garduño-Albino, R. A. Peralta, V. M. Trejos, L. Huerta Arcos, I. A. Ibarra, D. Solis-Ibarra, S. Cordero-Sánchez, N. S. Portillo-Vélez and J. M. Esparza-Schulz, *Dalton Trans.*, 2024, **53**, 12208–12214.
12 A. López-Olvera, J. A. Zárate, J. L. Obeso, E. Sánchez-González, J. A. De Los Reyes, R. A. Peralta, E. González-Zamora and I. A. Ibarra, *Inorg. Chem.*, 2023, **62**, 20901–20905.
13 Y. Liu, Y. Liu, L. Gu, J. Han, W. Zhi, Y. Wang and L. Wang, *Colloids Surf., B*, 2021, **208**, 112099.
14 Z. Guan, S. Zhu, S. Ding, D. Xia and D. Li, *Chemosphere*, 2022, **299**, 134481.
15 J.-T. Lu, H. Huang, H. Wu, S.-P. Wen, K.-Y. Gao, X.-L. Wu and Z.-R. Nie, *Rare Met.*, 2023, **42**, 672–679.
16 D. Yong, J. Tian, R. Yang, Q. Wu and X. Zhang, *Chin. J. Chem.*, 2024, **44**, 1343.
17 S. Sangeetha and G. Krishnamurthy, *Bull. Mater. Sci.*, 2020, **43**, 269.

18 Z. Li, D. Jia, W. Zhang, Y. Li, M. Wang and D. Zhang, *Front. Chem. Sci. Eng.*, 2024, **18**, 31.
19 P. Wang, X. Bian and Y. Li, *Chin. Sci. Bull.*, 2012, **57**, 33–40.
20 J.-X. Cui, Q. Luo, Z.-G. Zhang, J.-T. Zhu and B.-L. Shen, *Rare Met.*, 2023, **42**, 3430–3442.
21 M. Lammert, M. T. Wharmby, S. Smolders, B. Bueken, A. Lieb, K. A. Lomachenko, D. D. Vos and N. Stock, *Chem. Commun.*, 2015, **51**, 12578–12581.
22 A. Sharma, S. Bedi, K. Verma, B. Lal, V. John, R. Kumar, S. Kaushal and R. Badru, *Polyhedron*, 2023, **242**, 116517.
23 I. Rangel-Vázquez, G. Del Angel, E. Ramos-Ramírez, P. Acevedo-Peña, C. Martínez Gómez, F. Tzompantzi, N. Gutiérrez Ortega and J. G. Torres-Torres, *RSC Adv.*, 2023, **13**, 19832–19845.
24 E. Peralta, G. Roa, J. A. Hernandez-Servin, R. Romero, P. Balderas and R. Natividad, *Electrochim. Acta*, 2014, **129**, 137–141.
25 J. Li, Y. Fan, R. Zhang, D. Ban, Z. Duan, X. Liu and L. Liu, *Mater. Chem. Front.*, 2024, **8**, 3509–3527.
26 F. Keshavarz, V. Kavun, M. A. Van Der Veen, E. Repo and B. Barbiellini, *Chem. Eng. J.*, 2022, **440**, 135905.
27 E. F. Pettersen, T. D. Goddard, C. C. Huang, G. S. Couch, D. M. Greenblatt, E. C. Meng and T. E. Ferrin, *J. Comput. Chem.*, 2004, **25**, 1605–1612.
28 J. B. Maglic and R. Lavendomme, *J. Appl. Crystallogr.*, 2022, **55**, 1033–1044.
29 K. Chakarova, I. Strauss, M. Mihaylov, N. Drenchev and K. Hadjiivanov, *Microporous Mesoporous Mater.*, 2019, **281**, 110–122.
30 S. Bargozideh, M. Tasviri, S. Shekarabi and H. Daneshgar, *New J. Chem.*, 2020, **44**, 13083–13092.
31 Y. L. Wang, S. Zhang, Y. F. Zhao, J. Bedia, J. J. Rodriguez and C. Belver, *J. Environ. Chem. Eng.*, 2021, **9**, 106087.
32 A. Loosen, C. Simms, S. Smolders, D. E. De Vos and T. N. Parac-Vogt, *ACS Appl. Nano Mater.*, 2021, **4**, 5748–5757.
33 C. S. Cox, E. Slavich, L. K. Macreadie, L. K. McKemmish and M. Lessio, *Chem. Mater.*, 2023, **35**, 3057–3072.
34 K. Nikoofar and Z. Khademi, *Res. Chem. Intermed.*, 2016, **42**, 3929–3977.
35 Y. Wang, N. Zhang, R. Wang, Y. He, H. Zhou, X. Li, G. Gao, H. Sun and X. Liu, *Dalton Trans.*, 2023, **52**, 10079–10088.
36 B. Guo, T. Xu, L. Zhang and S. Li, *J. Environ. Manage.*, 2020, **272**, 111047.
37 H. Chen, C. Liu, W. Guo, Z. Wang, Y. Shi, Y. Yu and L. Wu, *Catal. Sci. Technol.*, 2022, **12**, 1812–1823.
38 K. Zhou, Y. Zhang, M. Liu, Z. Zhao, X. Liu, Z. Bao, Q. Yang, Q. Ren and Z. Zhang, *Catal. Sci. Technol.*, 2024, **14**, 1605–1612.
39 D. Chen, H. Sun, Y. Wang, H. Quan, Z. Ruan, Z. Ren and X. Luo, *Appl. Surf. Sci.*, 2020, **507**, 145054.
40 E. E. Ghadim, M. Walker and R. I. Walton, *Dalton Trans.*, 2023, **52**, 11143–11157.